JGR Atmospheres

RESEARCH ARTICLE
10.1029/2023JD039681

Special Section:
Dust and dust storms: From physical processes to human health, safety, and welfare

The Relationship Between the Saharan Air Layer, Convective Environmental Conditions, and Precipitation in Puerto Rico

P. W. Miller[1,2] **and C. Ramseyer**[3]

[1]Department of Oceanography and Coastal Sciences, Louisiana State University, Baton Rouge, LA, USA, [2]Coastal Studies Institute, Louisiana State University, Baton Rouge, LA, USA, [3]Department of Geography, Virginia Tech, Blacksburg, VA, USA

Key Points:

- Saharan air layer (SAL) patterns are resolved by a self-organizing map of daily column-integrated dust flux fields during June and July
- The SAL's footprint coincides with a region of poor convective precipitation environments for the most westward-protruding patterns
- Puerto Rico experiences island-wide precipitation deficits on days characterized by an active SAL extended toward the Caribbean

Supporting Information:

Supporting Information may be found in the online version of this article.

Correspondence to:

P. W. Miller,
pmiller1@lsu.edu

Citation:

Miller, P. W., & Ramseyer, C. (2024). The relationship between the Saharan air layer, convective environmental conditions, and precipitation in Puerto Rico. *Journal of Geophysical Research: Atmospheres*, *129*, e2023JD039681. https://doi.org/10.1029/2023JD039681

Received 19 JUL 2023
Accepted 12 DEC 2023

Author Contributions:

Conceptualization: C. Ramseyer
Funding acquisition: C. Ramseyer
Methodology: C. Ramseyer
Writing – original draft: C. Ramseyer

Abstract The Saharan Air Layer (SAL) is a hot, dry, and dust-laden feature that advects large concentrations of dust across the Atlantic annually to destination regions in the Americas and Caribbean. However, recent work has suggested the SAL may be a contributing factor to high-impact drought in the Caribbean basin. While the SAL's characteristic dust loadings have been the focus of much previous research, fewer efforts have holistically engaged the co-evolution of the dust plume, its associated convective environment, and resultant rainfall in Caribbean islands. This study employs a self-organizing map (SOM) classification to identify the common trans-Atlantic dust transport typologies associated with the SAL during June and July 1981–2020. Using the column-integrated dust flux, termed integrated dust transport (IDT), from MERRA-2 reanalysis as a SAL proxy, the SOM resolved two common patterns which resembled trans-Atlantic SAL outbreaks. During these events, the convective environment associated with the SAL, as inferred by the Gálvez-Davison Index, becomes less conducive to precipitation as the SAL migrates further away from the west African coast. Simultaneously, days with IDT patterns grouped to the SAL outbreak typologies demonstrate island-wide negative precipitation anomalies in Puerto Rico. The SOM's most distinctive SAL outbreak pattern has experienced a statistically significant increase during the 40-year study period, becoming roughly 10% more frequent over that time. These results are relevant for both climate scientists and water managers wishing to better anticipate Caribbean droughts on both the long and short terms.

Plain Language Summary Saharan dust can be mobilized, lofted, and transported astonishingly vast distances from its African source regions to destinations in the Caribbean and Americas. While the movement of the dust through the atmosphere has important implications for ecological productivity and global climate trends, it can also acutely suppress tropical rainfall as it traverses the western Atlantic. This study finds that days with the most prominent extensions of Saharan dust toward the Caribbean were also less favorable for thunderstorm activity over the Atlantic Ocean and resulted in island-wide below-average rainfall in Puerto Rico. Additionally, the most prominent SAL outbreak days have become roughly 10% more common since 1981.

1. Introduction

Hot, dry, and dusty air advected westward from the Sahara (Figure 1), often termed the Saharan air layer (SAL), is a regular, yet variable, feature of tropical north Atlantic (TNA) climate. Because the SAL is an elevated layer of warm air, it produces statically stable thermodynamic conditions (Wong & Dessler, 2005) while also diminishing precipitable water values in the locations it affects (Dunion, 2011). Thus, in addition to acting as a capping inversion, the SAL promotes dry air entrainment within the elevated layer, further diminishing parcel buoyancy and preventing nascent updrafts from developing into deep moist convection (Miller et al., 2021). While the SAL has been shown to occupy several recurring pathways between the Sahara and the Americas (Doherty et al., 2008; Huang et al., 2010; Meng et al., 2017), the SAL's variability has recently garnered attention for its relationship with eastern Caribbean droughts and tropical rainfall suppression. For instance, Mote et al. (2017) showed that the historic 2015 drought in Puerto Rico developed in tandem with the arrival of several anomalously early and intense Saharan dust outbreaks. Similarly, Flores et al. (2023) noted the development of a strong capping inversion atop the marine boundary layer during a SAL outbreak observed during the 2013 SALTRACE field campaign.

Because eastern Caribbean islands are generally characterized by steep terrain and rocky soils, they are limited in both surface (i.e., large rivers and reservoirs) and groundwater resources. Consequently, these small islands quickly experience water resources strain whenever the region's regularly recurring precipitation deviates from its

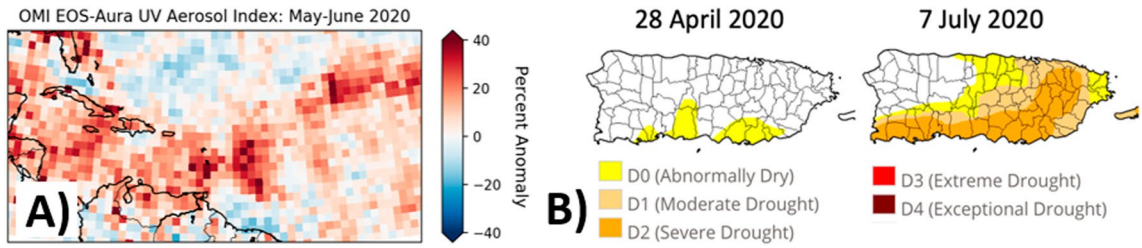

Figure 1. (a) Aerosol index anomaly over western Atlantic during May–June 2020 versus May–June 2011–2020 from the *Aura* Ozone Monitoring Instrument (OMI). (b) Change in the U.S. Drought Monitor over Puerto Rico from before and after the 2-month dusty period in (a).

climatological norm. Historically, drought research in the eastern Caribbean has centered on long-term drought, which has been tenuously associated warm phases of the El Niño-Southern Oscillation (ENSO) (Herrera & Ault, 2017; Moraes et al., 2022; Torres-Valcárcel, 2018). However, in recent years the rapid accumulation of drought conditions over short timescales in the U.S. Caribbean has become an increasing concern among water-sensitive sectors (Mercado-Díaz et al., 2023; Ramseyer & Miller, 2023). In June 2020, a widely publicized and well-studied Saharan dust event in the Caribbean (e.g., Yu et al., 2021) also coincided with the development of "severe drought" over parts of Puerto Rico according to the U.S. Drought Monitor (USDM, 2020). Figure 1a shows the May–June 2020 aerosol index anomalies measured by the Ozone Monitoring Instrument (OMI) over the western Atlantic, and Figure 1b illustrates the expansion of drought-afflicted area in Puerto Rico immediately before and after the 2-month dusty period in Figure 1a.

Though Mote et al. (2017) demonstrated the synchronicity between the SAL's arrival, diminished values of a tropical convective precipitation forecasting tool called the Gálvez-Davison Index (GDI), and resultant rainfall deficits during the 2015 drought, such an analysis has never been conducted on a long timescale. Even though other studies have likewise documented the relationship between the SAL and precipitation suppression (i.e., Flores et al., 2023; Wong & Dessler, 2005), these too are limited to case studies of individual SALs or single years. Meanwhile, Miller et al. (2019) resolved a long-term relationship between the GDI and Puerto Rico's early rainfall season productivity, though the GDI was not analyzed as a function of dust loadings over the region. Thus, it remains unknown the extent to which Saharan dust intrusions across the TNA are systematically associated with (un)favorable convective environments, and ultimately, acute rainfall deficits in water-limited Caribbean islands. The purpose of this study is to investigate the holistic relationship between dust transport within the TNA, coincident measures of convective rainfall favorability, and precipitation in Puerto Rico. This research will be valuable for understanding the hydrological impacts of distant dust outbreaks across water-vulnerable Caribbean islands.

2. Data and Methods

This study employs a self-organizing map (SOM) classification system (Kohonen, 1990) to discriminate between preferred modes of dust transport morphology (i.e., termed "nodes" is SOM nomenclature), which will be inferred to represent the SAL. After analyzing the temporal trends associated with each node and common node sequences, the observed daily rainfall over Puerto Rico is investigated under each SAL pathway.

2.1. Characterizing the SAL

SALs are identified by adapting a widely employed atmospheric river (AR) characterization technique to dust aerosols. Whereas ARs are defined as corridors of enhanced integrated vapor transport (IVT) (e.g., Debbage et al., 2017; Guan & Waliser, 2015), this study introduces integrated dust transport (IDT), a slight modification of the "aerosol ARs" defined by Chakraborty et al. (2021). In their adaptation, the zonal and meridional species-specific aerosol fluxes were accessed from the "tavg1_2d_aer_Nx – 2D" product series generated by NASA's Modern-Era Retrospective Analysis, version 2 (MERRA-2) (Gelaro et al., 2017). These data products contain both the hourly average u and v components of dust column mass flux (DUFLUXU and DUFLUXV in MERRA-2 nomenclature). Because this work is solely concerned with SAL-related dust transport, the "column dust mass flux" will be renamed IDT. The u and v components of IDT can easily be combined to yield the total vector IDT using Equation 1.

$$\mathrm{IDT} = \sqrt{\mathrm{IDT}_u{}^2 + \mathrm{IDT}_v{}^2} \tag{1}$$

IDT is computed at 0000 UTC for June–July between 1981 and 2020 at 0.5° × 0.625° spatial resolution, the standard grid spacing for MERRA-2. The IDT analysis is limited to June-July so that the SOM classification will be robust to inter-seasonal changes in dust loadings and better resolve different SAL patterns during a time of year it is most active (Dunion, 2011). The IDT calculation yields 2,440 inputs for the SOM.

2.2. SOM Initialization and Settings

SOMs are a machine learning classification technique whereby reference vectors are placed into a high-dimensional data space (i.e., MERRA-2 derived IDT) and fit to the input vectors using unsupervised classification and a vector quanitization algorithm (Kohonen, 1990). The self-organizing algorithm acts as a nonlinear projection of the probability distribution function of a high-dimensional input data set to a two-dimensional display. Through the training of the algorithm, the reference vectors are iteratively updated in the dataspace to minimize the error between the distance of the reference vectors and the input data vectors. This methodology allows for the classification of highly complex data sets into representative clusters. As such, SOMs have become an important tool for climate scientists, particularly those using reanalysis and satellite data sets (Hewitson & Crane, 2002; Reusch et al., 2005; Sheridan & Lee, 2011). More recently, SOMs have been extensively used to examine the tropical climate dynamics (Ramseyer et al., 2019; Ramseyer & Mote, 2018).

SOMs have been shown to have advantages over other classification techniques such as principal component analysis and empirical orthogonal functions (e.g., Reusch et al., 2005). One of the most significant advantages is the ability to preserve all of the input data in the final SOM. Practically speaking, this means all of the input data are mapped to a representative node, preserving even the most extreme data vectors and facilitating the analysis of low-frequency events. The training of the SOM was computed in Python using the scikit-som package, which is a SOM implementation of the similar scikit-learn package (Pedregosa et al., 2011). Scikit-learn has been implemented for machine learning modeling in climate science research (e.g., O'Gorman & Dwyer, 2018; Watt-Meyer et al., 2021). The trained SOM presented here is constructed with a user-selected 12 nodes, separated in a 3 × 4 rectangular lattice, which provides better results compared to SOMs with square dimensionality (Kohonen, 1990). The 12-node lattice allowed more extreme environments to still be represented by one of the nodes, while also preventing the SOM nodes from resolving nodes with too few representative input vectors. Additionally, fewer nodes resulted in a SOM that did not sufficiently represent higher IDT environments.

2.3. Thermodynamic Conditions

The thermodynamic environment associated with each SAL pattern is inferred using an operational convective rainfall forecasting tool called the Gálvez-Davison Index (GDI) (Gálvez & Davison, 2016). The GDI was developed by forecasters at the Weather Prediction Center to improve upon deficiencies experienced by mid-latitude-oriented stability indices (e.g., *k*-index, total totals, and convective available potential energy) by better capturing the mechanisms relevant to tropical precipitation. It is obtained by summing three component terms (Equation 2): the Column Buoyancy Index (CBI; Equation 3), the Inversion Index (II; Equation 4), and the Midlevel Warming Index (MWI; Equation 5), which are each computed using some combination of the equivalent potential temperature (θ_e) and air temperature (T) at 950, 850, 700, and 500 hPa. While the GDI's full derivation is too lengthy to reproduce here, Equations 3–5 provide abridged term definitions so the reader can understand the important physical inputs that influence each component. Readers can refer to Gálvez and Davison (2016) for a comprehensive GDI explanation and definition.

$$\mathrm{GDI} = \text{Column Buoyancy Index (CBI)} + \text{Inversion Index (II)} + \text{Midlevel Warming Index (MWI)} \tag{2}$$

$$\mathrm{CBI} = f(\theta_{e\,950}, \theta_{e\,500}) \tag{3}$$

$$\mathrm{II} = f\left(T_{950}, T_{700}, \theta_{e\,950}, \bar{\theta}_{e\,850-700}\right) \tag{4}$$

$$\mathrm{MWI} = f(T_{500}) \tag{5}$$

Though developed as a near-term operational forecasting tool, the GDI has been shown to successfully represent favorable precipitation conditions on both daily and seasonal timescales in Puerto Rico (Miller et al., 2019) and has even proved effective in future climate downscaling studies for the region (Ramseyer et al., 2019). Critically,

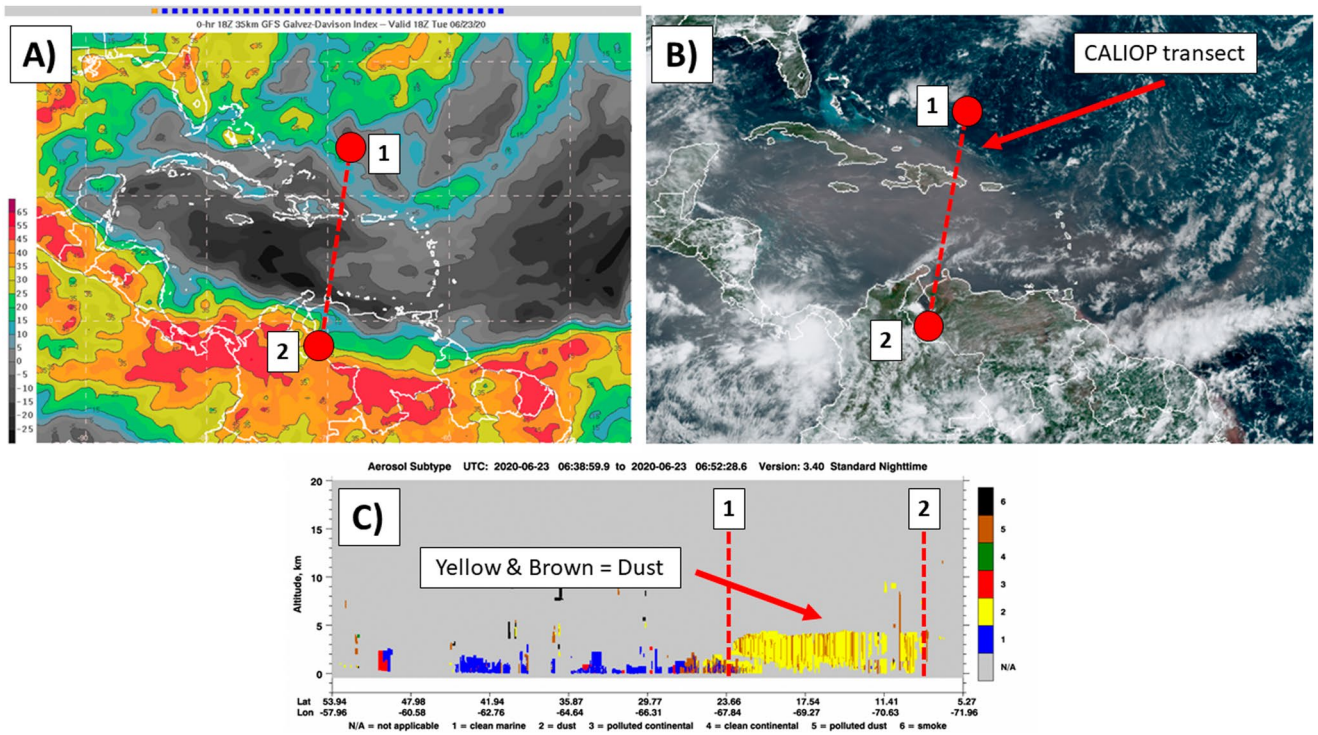

Figure 2. (a) GDI forecast from the Weather Prediction Center (https://www.wpc.ncep.noaa.gov/international/gdi/) for 1800 UTC on 23 June 2020 during the passage of a strong SAL. Warm hues indicate strong potential for rainfall and gray/black hues indicate rain is unlikely. (b) Coincident GOES-16 visible image with dust indicated as hazy, slightly opaque pixels. (c) CALIOP aerosol transect from the CALIPSO platform for 0600 UTC 23 June with start and endpoints labeled. The low GDI region in (a) is accompanied by visually hazy, brown conditions in (b), which also possess scattering regions characteristic of dust aerosols in (c).

one of the three component terms, the II, was shown by Mote et al. (2017) to be sensitive to the presence of the hot, dry SAL yielding depressed values of the GDI within its vicinity (Miller & Ramseyer, 2020; Miller et al., 2021). The II term combines the 950–700-hPa temperature lapse rate with the θ_e lapse rate between 950 hPa and the 850–700-hPa mean layer. Whereas temperature lapse rate can capture the convective inhibition arising from an inversion layer, the θ_e lapse rate can provide additional information about the stabilizing effects of dry air entrainment among rising updrafts. Upon its approach to the Caribbean, the SAL's elevated hot, dry air mass should be well captured by the II.

Figure 2 shows an example of the GDI and its relationship to Saharan dust concentrations during the "Godzilla" dust plume from June 2020 (Asutosh et al., 2022; Francis et al., 2020; Pu & Jin, 2021; Yu et al., 2021). GDIs less than 5 (Figure 2a), indicating only a limited likelihood of shallow convection and trace rainfall accumulations (Gálvez & Davison, 2016), correspond to the SAL as seen by both visible dust concentrations (Figure 2b) and remotely sensed aerosol-scattering profiles (Figure 2c).

Daily 0000-UTC GDI was calculated from the ERA5 data set (Hersbach et al., 2020) following the relationships described in Gálvez and Davison (2016) for the same 2-month (June–July) and 40-year period (1981–2020) as the MERRA-2 IDT fields. In their analysis of the June 2020 Saharan dust outbreak, Pu and Jin (2021) showed that MERRA-2 and ERA5 reanalyses provided similar representations of the meteorological conditions associated with the SAL.

2.4. Precipitation Analysis

Daily rainfall totals were retrieved from the Daymet precipitation data set, version 4 (Thornton et al., 2017). Daymet is a 1-km gridded product covering all of North America as well as Hawaii, Alaska, and Puerto Rico. Thornton et al. (1997) reported a mean absolute error of 19.3% for the predicted annual rainfall totals at Global Historical Climatology Network-Daily (GHCN-Daily) stations used to generate the product. Daily precipitation totals were binned by their best-matching node in the SOM and used to compute a node-specific average. These

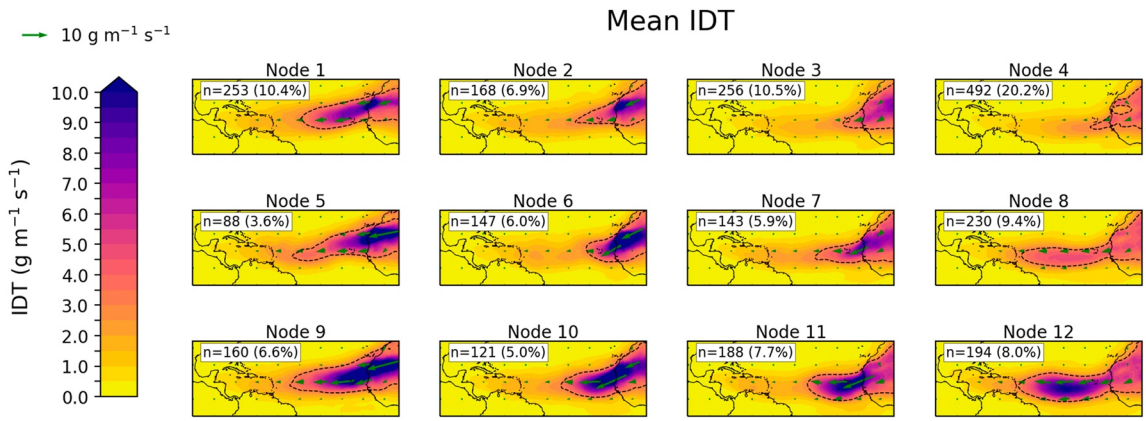

Figure 3. SOM of daily IDT during June–July 1981–2020. Deep orange and purple hues indicate a likely SAL presence with the 3 g m^{-1} s^{-1} contour is drawn in a dashed black line. The number of days grouped to each node is shown in the upper-left corner of each pane.

daily node means are also compared to the June–July 1981–2020 overall daily mean to derive a daily node anomaly.

3. Results and Discussion

3.1. Trans-Atlantic SAL Pathways

Figure 3 shows the results of the SOM classification with Figure S1 in Supporting Information S1 confirming the presence of stronger dust loading along these pathways using the daily OMI Aerosol Index between 2005 and 2020. The most common pattern in the data set, node 4, is the best match for 20.2% of days and represents a low-IDT environment over much of the western Atlantic. Nodes 2, 3, and 6, while possessing greater IDT over north Africa, display little dust advection into the Atlantic basin. Together, these relatively dust-dormant nodes constitute 43.6% of all June–July days. In contrast, nodes 5, 8, 9, and 12, resolve a more SAL-like pattern with a more consolidated corridor of high IDT stretching from north Africa toward the Caribbean. Each of the IDT nodes resolved in Figure 3 resemble the summertime dust transport axis identified by Meng et al. (2017) using 15 years of MODIS AOD observations.

Nodes 8 and 12 exhibit similar spatial IDT distributions, differentiated only by the intensity of their IDT. These nodes show the furthest westward progression of the 3-g m^{-1} s^{-1} contour, which abuts the Lesser Antilles and even captures Barbados in the case of node 12. Together, these two patterns represent 17.4% of the mid-summer days. Notably, node 12, and to a lesser extent node 8, demonstrate a displacement between their largest IDT values located over the Atlantic and the dust source region in north Africa. The 3-g m^{-1} s^{-1} contour also narrows slightly as it crosses the west African coastline further indicating the plume of largest IDT has migrated offshore. Morphologically, these patterns are consistent with a SAL outbreak that has exited the Saharan and is advecting across the Atlantic, with node 12 representing a more severe dust outbreak than node 8. In fact, some of the well-known SAL outbreaks, such as the example in Figure 2 and the June 2015 episode studied by Miller et al. (2021), were grouped to node 12. During the 2015 drought, node 12 was detected on 11 days, more than double its 40-year mean of 5.1 instances per year.

The SOM can also characterize the temporal evolution of the IDT plume. For instance, 4 days after being grouped to node 11, 16.2% of IDT patterns migrate to node 8 and 18.5% to node 12. This means that 34.7% of high IDT patterns over the Cabo Verde islands continue westward across the Atlantic, whereas another 31.8% of node 11 days migrate to node 4 after 4 days, indicating a termination of the IDT event (The remaining one third of node 11 patterns is dispersed across the other nine nodes.) Figure S2 in Supporting Information S1 shows the full complement of node migrations after 4 days.

Figure 4 plots the annual time series of the SOM node frequencies during the 40-year study period. Whereas most node trends are static, node 12, the SAL outbreak pattern, has become significantly more frequent with 95% confidence. Based on the fitted trend line, these patterns have increased by 6 yr^{-1} since 1981, which represents roughly 10% of the June–July seasonal period analyzed. Node 11 has also increased significantly, but by a smaller

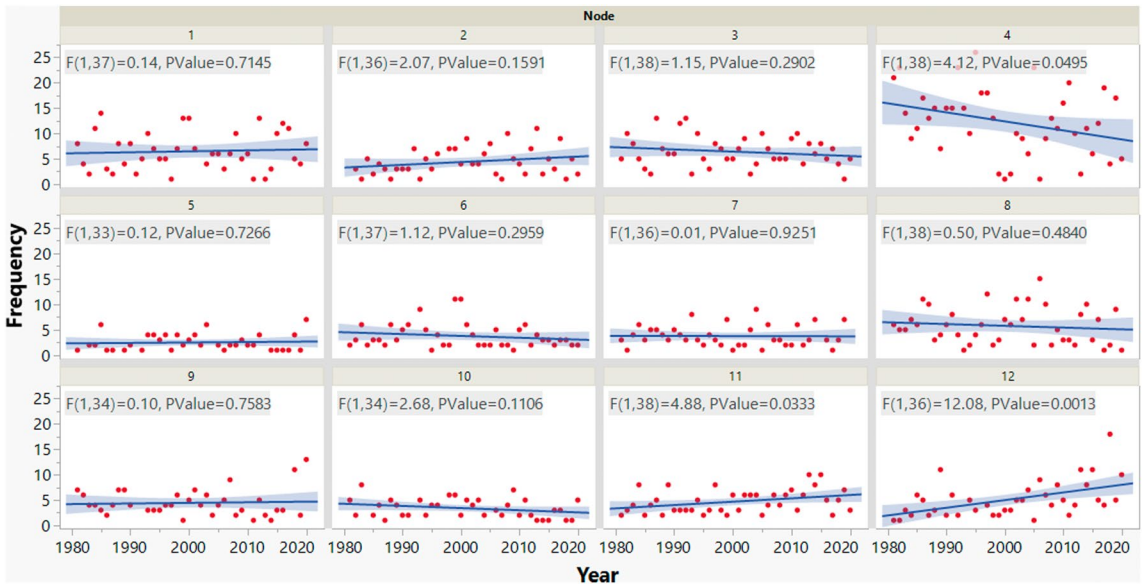

Figure 4. Time series of annual node frequency. Least squares regression trend lines are plotted in blue with the 95% confidence interval of the fit indicated by transparent blue shading. The *F* statistic and *p*-value for the fit are reported in the upper left of each pane.

margin of only 2.6 yr^{-1}. The gains in the active SAL nodes have been necessarily offset by significant decreases in the most benign IDT pattern, node 4, which has receded by 7.1 yr^{-1}.

3.2. GDI Conditions During SAL Patterns

The mean GDI regimes coincident with the 12 IDT patterns (Figure 3) are shown in Figure 5. Overall, the patterns are characterized by the same basic features including a filament of high GDIs associated with the ITCZ in the southern tier of the domain. Additionally, each node shows a southwest-to-northeast corridor of low GDI values across the central TNA, which aligns closely with a region of frequent April-July trade-wind inversions identified by Ramseyer and Miller (2021). For several of the higher IDT patterns (e.g., nodes 9, 10, and 11), the 3-g m^{-1} s^{-1} IDT contour forms the edge of this low-GDI region in the central TNA, suggesting that the SAL's westward progression is tied to the position and strength of North Atlantic subtropical high (NASH)-related subsidence (Colarco et al., 2003). Pu and Jin (2021) show that the anomalous strength of the NASH in June 2020 was key to transporting Saharan dust into the Southeastern United States. Similarly, Doherty et al. (2008) associated a westward displacement of the NASH with elevated Saharan dust transport across the Atlantic along its northerly route.

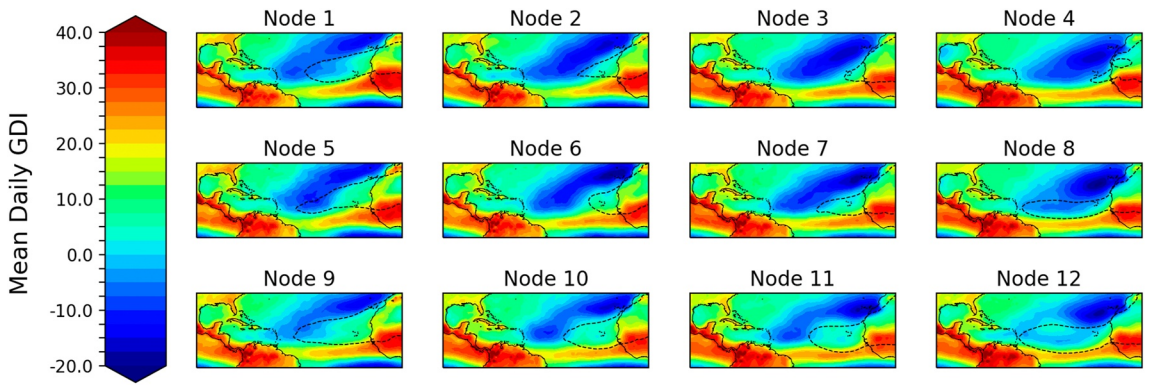

Figure 5. Mean GDI for each of the 12 IDT patterns identified. The 3-g m^{-1} s^{-1} IDT contour is drawn in a dashed black line as in Figure 3.

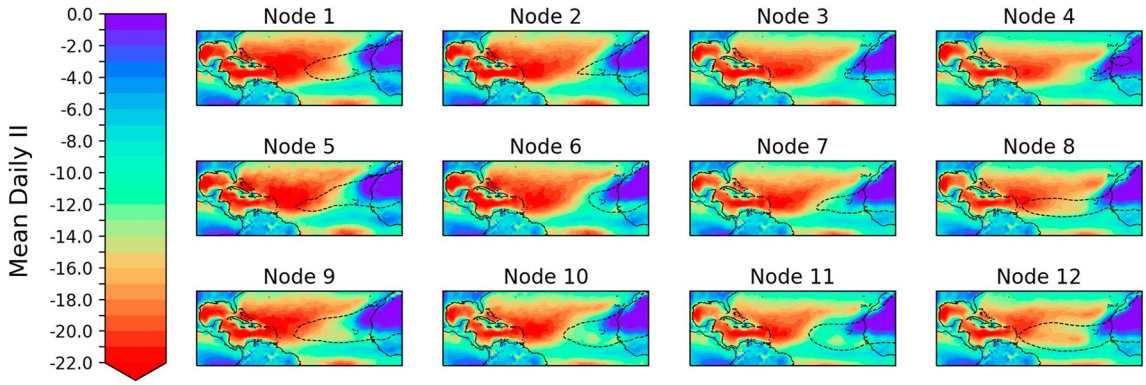

Figure 6. Mean II for each of the 12 IDT patterns identified in Figure 3. The 3-g m^{-1} s^{-1} IDT contour is drawn in a dashed black line as in Figure 3.

In the case of node 12, the most pronounced SAL outbreak pattern, the lowest GDI values are confined to the northeast corner of the domain, while the 3-g m^{-1} s^{-1} IDT contour extends all the way to Barbados. However, the center of the dust plume is characterized by a depression in GDI, a pattern that can also be discerned, though less clearly, in node 8. Because the II term of the GDI calculation is sensitive to the presence of hot, dry air between 950 and 700 hPa, this term would intuitively decrease as the SAL descends more completely into these layers as it advects westward across the Atlantic (Kuciauskas et al., 2017). In fact, several other IDT patterns (nodes 1, 5, and 9) indicate a signature consistent with gradually decreasing GDIs as the SAL extends further away from its source region.

Figure 6 explores the mean state of the II term for each pattern to more directly investigate the stabilizing presence of the SAL. Indeed, the tongues of depressed GDI values noted in several patterns above coincide with more strongly negative values of the II, which in turn, reduce the GDI. Nodes 1, 5, and 9 each show a transition from near-zero II over the west African coast to less than −20 II west of the Cabo Verde islands within the 3-g m^{-1} s^{-1} IDT contour. Meanwhile, nodes 8 and 12 possess less than −15 IIs within the bulb of the westward-migrating IDT that is pseudo-detached from the source region. Thus, the most westward-propagating IDT plumes reduce convective potential by increasing low-level inhibition and promoting dry-air entrainment.

The June 2020 Saharan dust outbreak is examined in more detail to see how the GDI varies with IDT on a more granular temporal scale (Figure 7). As the IDT plume emerges off the African coast on 18 June 2020, it is accompanied by >20 GDI and near-zero II. By 19-20 June, a small area of depressed GDI and II has developed on the southern flank of the 10-g m^{-1} s^{-1} IDT contour. As the Saharan dust front approaches the eastern Caribbean islands on 21 June, the leading edge of the plume is characterized by highly negative GDI values driven by decreases in the II. From this point forward, the SAL within the 10-g m^{-1} s^{-1} IDT contour is associated with highly stable air as indicated by the GDI and its component II term. During this time frame, this pulse of high IDT begins interacting with a precedent, existing area of low GDI over the Caribbean Sea. In the wake of the high IDT lies a residual low GDI environment likely the result of dust settling and/or increased warming and subsidence from the subtropical high. The decline in the GDI accelerates significantly beginning on 21 June 2020, the same day that the IDT pulse also begins to weaken, reflecting either a reduction in dust concentrations due to settling, or a weakening in the wind speeds that drive the flux terms in Equation 1.

3.3. Eastern Caribbean Precipitation

As described in Section 1, the motivation of understanding SAL pathways into the Caribbean is driven by its connection to rainfall and potentially drought. For each IDT pattern in Figure 3, the daily rainfall anomaly for Puerto Rico was computed against the June-July 1981–2020 mean to show which nodes are responsible for daily precipitation declines. While all eastern Caribbean islands are particularly vulnerable to drought, Puerto Rico is the only location for which the 1-km daily Daymet precipitation product is available. Figure 8 shows that most of the IDT patterns are associated with a mixed combination of above- and below-average daily precipitation for Puerto Rico. Only two nodes, 8 and 12, are associated with homogeneous anomalies of any sign across the whole island. Both of these patterns, which are determined from Figure 3 to show trans-Atlantic SAL outbreaks,

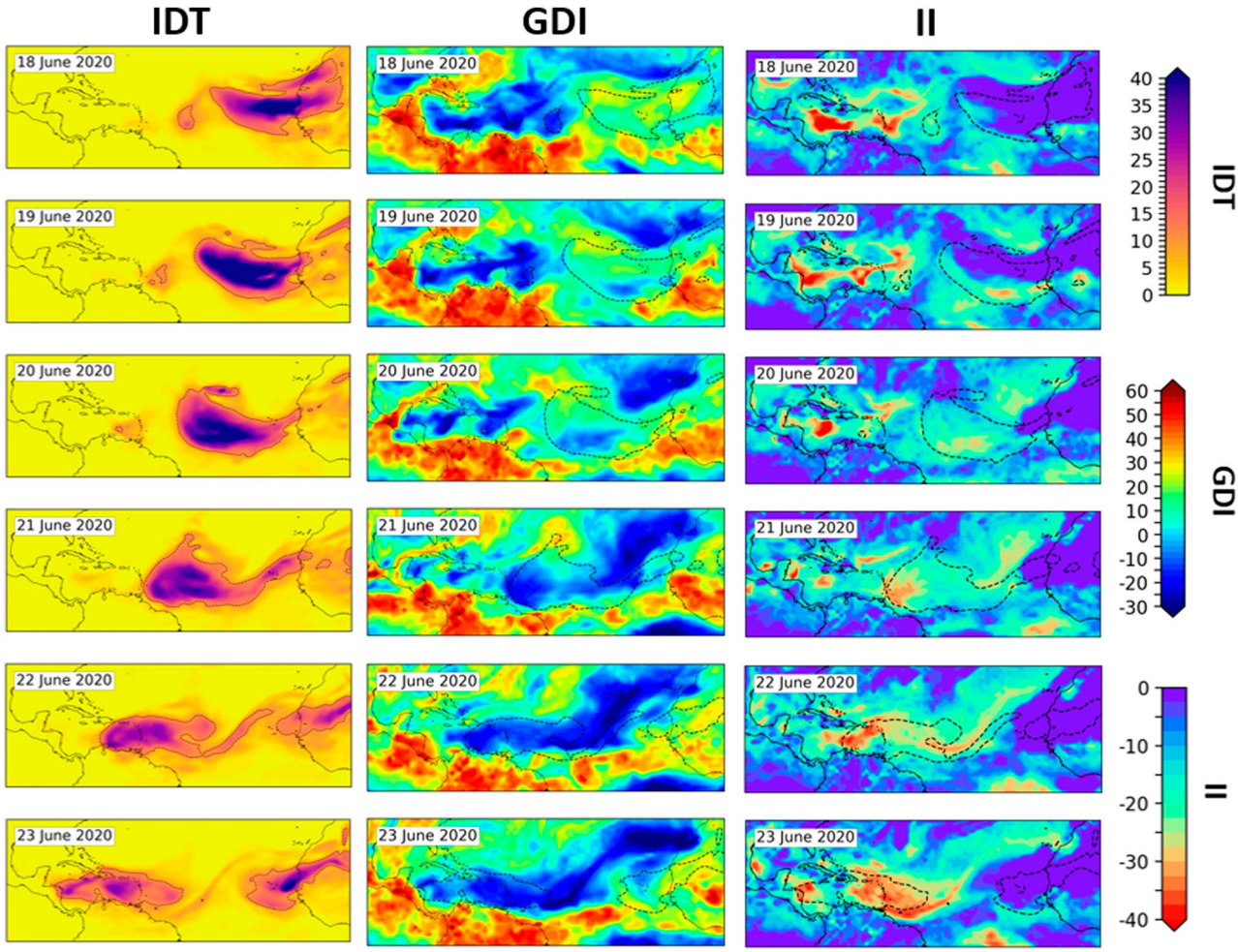

Figure 7. Daily IDT, GDI, and II between 18 and 23 June 2020 coinciding with a significant Saharan dust outbreak. The 10-g m^{-1} s^{-1} IDT contour is drawn in all three variables as a black dashed line. All days above were grouped to node 12 except for 18 and 23 June when the IDT distributions were briefly sorted to nodes 9 and 10, respectively.

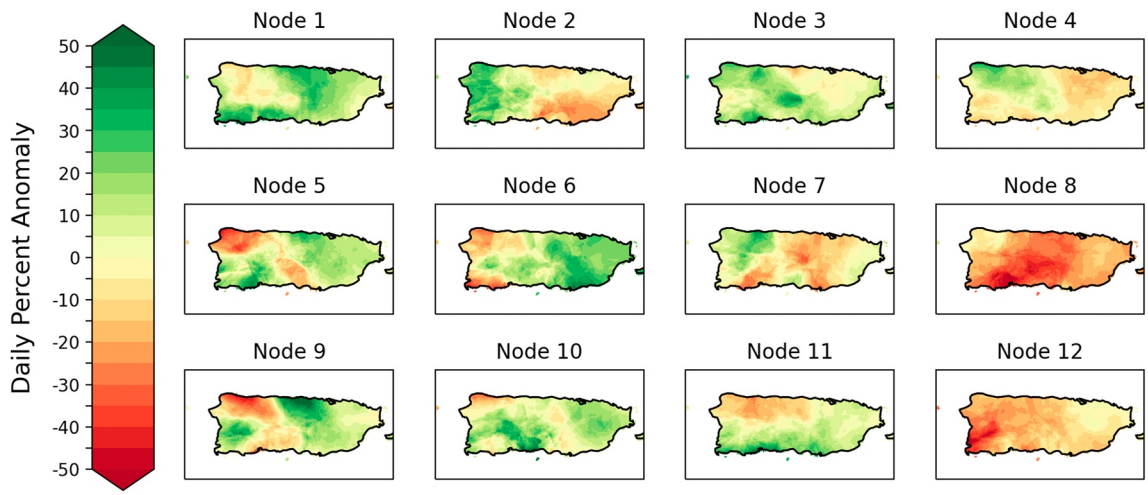

Figure 8. Mean daily precipitation anomaly compared to the 40-year June–July average for each of the 12 IDT patterns identified in Figure 3.

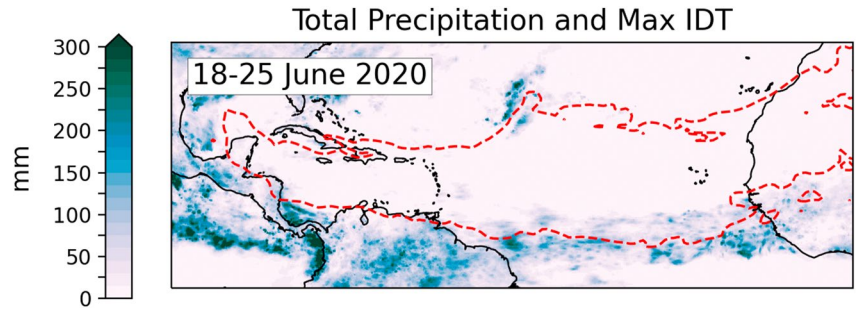

Figure 9. Total 8-day precipitation during the SAL outbreak shown in Figure 7. The maximum extent of the 10-g m^{-1} s^{-1} IDT contour is drawn by red dashes.

depict island-wide below-average precipitation. Figure 9 shows the 8-day total precipitation from NASA's final-run IMERG product (Huffman et al., 2014) during the June 2020 SAL outbreak from Figure 7. While some precipitation is observed along the lefthand flank of the migrating SAL, the central SAL axis is largely devoid of precipitation. In fact, the 10-g m^{-1} s^{-1} IDT contour carves out a near-perfect boundary between the precipitating and non-precipitating regions over northern South America, Central America, and the Gulf of Mexico.

One of the unique characteristics of the 2015 Puerto Rico drought documented by Mote et al. (2017) was the early arrival of Saharan dust in the Caribbean basin, well ahead of its typical active period. To systematically assess the hydrometeorological implications of earlier-than-normal SAL activity, May IDT fields for the 1981–2020 period were classified to the node structure using the same SOM that yielded Figure 3. Intuitively, most May days should be assigned to the least dust-active nodes, like 3 or 4, given that dust transport is still approaching its seasonal maximum. Indeed, this is the case with 9.7% and 74.5% of May IDT fields being paired with nodes 3 and 4, respectively, each year (Figure S3 in Supporting Information S1). Meanwhile, nodes 8 and 12, the apparent dust outbreak nodes, are much less common in May. Only 5.2% of May days associate to node 8 annually with 21 of the 40 years never even documenting such an IDT pattern. Node 12 is even more rare in the early summer, with 28 years devoid of this SAL configuration, and only 1.9% of May days resembling these SAL outbreaks. However, during the Puerto Rico drought of 2015, the fraction of May days paired to node 8 (22.6%) is >4x greater than the 1981–2020 average (Figure S3 in Supporting Information S1). While the correlation between May days paired to nodes 8 and 12 days and the island-mean concurrent precipitation is weak (not shown), Mays with a large proportion of days mapped to these nodes are exclusively dry. For instance, only 4 years encountered >20% of May days classified to nodes 8 or 12 combined: 1989, 2003, 2015, and 2017. According to the Daymet data set, Puerto Rico experienced below-averaged island-wide May precipitation anomalies on all of these years (−35.1%, −45.5%, −50.2%, and −13.4%, respectively) relative to the 1981–2020 average of 197 mm.

3.4. Dust-GDI-Precipitation Relationships

The IDT pathways, visualized through the SOM, and their associated GDI, II, and precipitation composites reveal consistent relationships between the presence of trans-Atlantic dust advection and diminished precipitation potential. Interestingly, the presence of a strong IDT signature in the eastern TNA did not depress GDI values, and in fact, appears to elevate them. This counter-intuitive finding illustrates the care that must be taken with interpreting a low GDI to correspond to the presence of a SAL. Figures 3, 5, and 6 together indicate that the SAL does appear to increasingly deteriorate the GDI as the pulse progresses across the Atlantic, such that low GDI and II values near and over the Caribbean may indeed represent a transient SAL outbreak.

Two mechanisms may be responsible for this dichotomous GDI response in regions of high IDT: The derivation of the GDI and the surface-pointing slope of the SAL along an east-to-west transect. Figures 5 and 6 showed that the depression in the GDI (Figure 5) among the SAL outbreak nodes (Figure 3; nodes 8 and 12) was largely driven by strongly negative II values (Figure 6). However, the II values were near-zero over the heaviest IDT zones across the Saharan source region, which led to unexpectedly large GDIs (~10) over one of the most arid regions of the planet. Because the II term is partially based on the 950–700-hPa temperature lapse rate (Equation 4), the extreme desert temperatures nearer the surface at 950 hPa (Figure 10) yield a large temperature change, even though extreme low relative humidity over the desert effectively precludes the possibility of deep

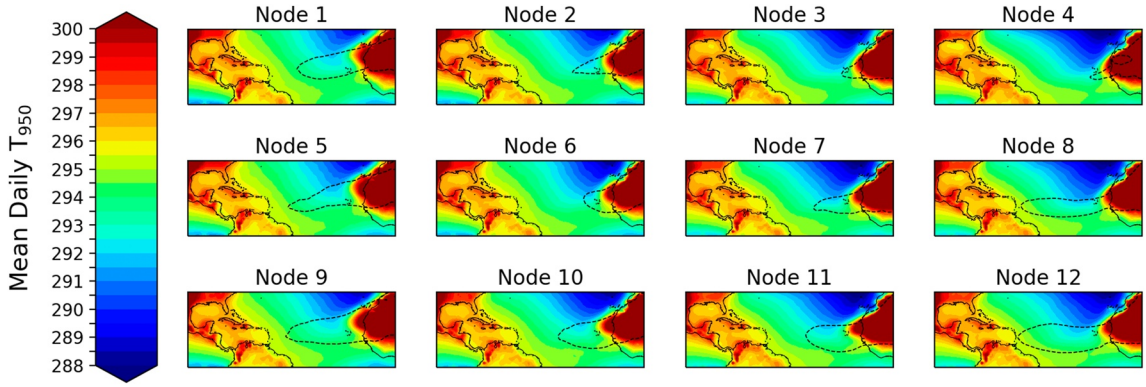

Figure 10. Mean 950-hPa temperature (K) for each of the 12 IDT patterns identified in Figure 3. The 3-g m^{-1} s^{-1} IDT contour is drawn in a dashed black line as in Figure 3.

moist convection. Additionally, the 850-hPa temperature, which most closely mirrors the SAL (Figure 11) is not directly included in the II calculation where it might indicate a SAL-related stable layer.

These structural limitations of the GDI near the dust source region are likely a by-product of its application outside the settings for which it was developed. While the GDI was designed to outperform mid-latitude-centric stability indices in the tropics, its accuracy is nonetheless optimized for the Caribbean (Gálvez & Davison, 2016). While the index has been successfully applied in settings outside this target region, such as northern Mexico (Pineda-Martínez et al., 2020), the Amazon (Lobato, 2019), the Congo Basin (Alber et al., 2021), and the Gulf of Mexico (Glenn, 2022), the Sahara likely pushes the limits of its transferability, despite its encroachment as far south as 16°N (Tucker et al., 1991). Future work may seek to develop a GDI variant that performs more accurately near dust source regions.

Further, the vertical dimensions of the SAL evolve as it transits the Atlantic (Kuciauskas et al., 2017), complicating its thermodynamic signature in GDI fields. Consequently, the hot, dry character of the SAL will more completely occupy or vacate the pressure levels used to calculate the GDI (950, 850, 700, and 500 hPa; Equations 3–5) as it progresses westward. Figures 10–12 show that the elevated air temperatures associated with the SAL are present at 950, 850, and 700 hPa over the dust source region. However, as the SAL is undercut by the marine boundary layer over the eastern TNA (Rittmeister et al., 2017), its hot, dry signature is no longer apparent at 950 hPa, allowing the 950–700-hPa temperature lapse rate to better reflect the presence of an elevated warm, stable layer and reduce the II (Figure 6). Meanwhile, Figure 12 shows that the thermal signature of the SAL does not extend as far westward at 700 hPa as it does at 850 hPa (Figure 11). For instance, in node 12, the 700-hPa temperature gradient outlining the SAL becomes diffuse and difficult to identify approximately midway across the TNA (Figure 12). In contrast, the 850-hPa temperature gradient extends effectively to the edge of the 3-g m^{-1} s^{-1} IDT contour (Figure 11). Thus, the SAL's descent below 700 hPa, while persisting at 850 hPa, may

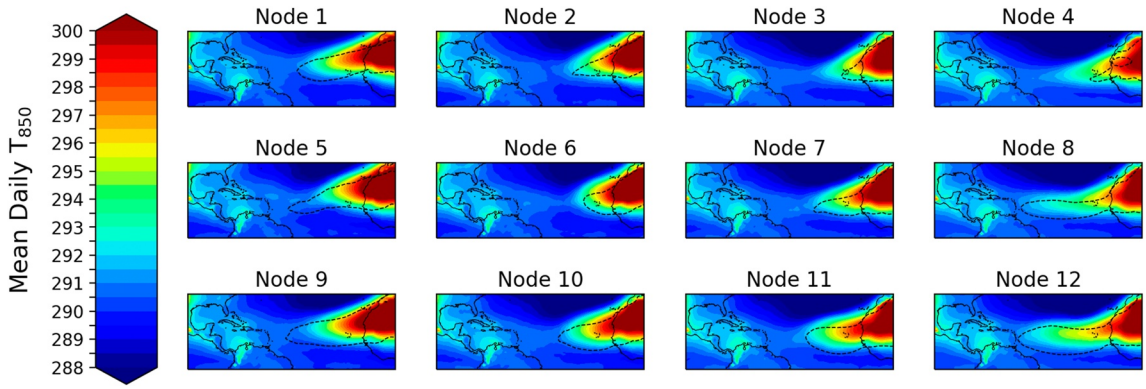

Figure 11. Mean 850-hPa temperature (K) for each of the 12 IDT patterns identified in Figure 3. The 3-g m^{-1} s^{-1} IDT contour is drawn in a dashed black line as in Figure 3.

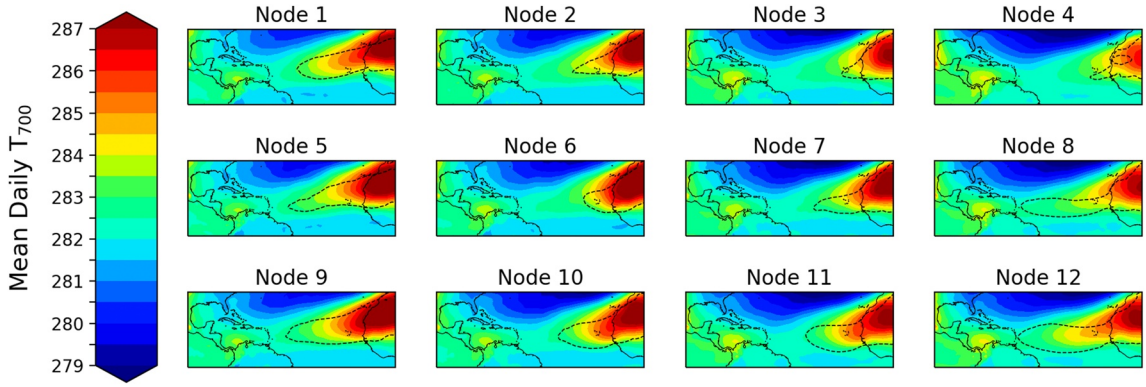

Figure 12. Mean 700-hPa temperature (K) for each of the 12 IDT patterns identified in Figure 3. The 3-g m^{-1} s^{-1} IDT contour is drawn in a dashed black line as in Figure 3.

allow the II to better detect the poor thermodynamic environment associated with it, as the plume approaches the Caribbean.

The zonally oriented slope to the SAL is well documented by studies focusing on the SAL's dust signatures. In a 5-year study of CALIOP lidar transects of SAL events, Tsamalis et al. (2013) documented a clear vertical evolution to the SAL as it journeys westward over the Atlantic. During June–July–August, the SAL descended from an altitude between 1 and 5 km over Africa to 0–2 km over the Gulf of Mexico. When standardized for the geometrical displacement, the SAL's thickness diminished by 9 m deg^{-1} west of 30°W while its mean altitude descended by 28 m deg^{-1} (Tsamalis et al., 2013). With Puerto Rico's longitude of 66°W, the mean SAL altitude will sink approximately 1 km after crossing 30°W as it moves toward the Caribbean [that is, (66°W–30°W) × 28 m deg^{-1} = 1,008 m]. Such compaction and descent were also prominently evident during the SALTRACE field campaign conducted in 2013, when the SAL was observed to evolve from occupying the 0.5–4.5-km layer off the coast of Africa to the 1–2-km layer just west of Barbados (Rittmeister et al., 2017). More recently, Pu and Jin (2021) used CALIOP lidar transects to show that the June 2020 dust outbreak depicted in Figure 7 descended from 2 to 6 km on 18 June to 2–5 km on 21 June and lastly 0–4 km on 23 June 2020 as it crossed the central Caribbean.

However, poor GDI environments, even in the Caribbean, can easily develop in the absence of a SAL. Figure 5 shows that most nodes demonstrate low GDI conditions over the eastern Caribbean even while the SAL is still positioned over the eastern TNA in Figure 3. In these cases, the low GDI is related to the detrimental contribution of the trade-wind inversion, which leads to a highly negative II term (Figure 6). Whereas Mote et al. (2017) interpreted the anomalously low II values across the TNA during April 2015 to represent an active, early season SAL, it appears they might have alternatively arisen due to the presence of a strong TWI in the early months of the drought. Meanwhile, the persistence of the poor GDI environment into mid-to-late summer that prevented any drought recovery, were more likely tied to the multiple dust outbreaks which were documented by Puerto Rico's AERONET site (Mote et al., 2017). Because low GDI in the Caribbean can be confounded by TWI, which is related to the strength and position of the NASH, the attribution of low GDI to large-scale forcing from the subtropical high versus regionalized influence from the SAL will be a focus of future study.

While the IDT composites for the SAL outbreak nodes, 8 and 12, resolve the greatest IDT well east of Puerto Rico, Figure 7 shows that individual days grouped to these patterns contain high IDT well into the Caribbean. The intrusion of SAL events into this region is well resolved by a low II and, by extension, a low GDI. This case study from June 2020 illustrates why nodes 8 and 12 in the IDT SOM also force the least amount of daily precipitation over Puerto Rico: While the composite IDT core may remain far from the island, individual events grouped to these patterns propagate much closer, deteriorating precipitation conditions as they approach. Additionally, environments where the IDT core remains east of the island likely represent situations where mesoscale convective growth upwind of the island is limited and thus is reliant on local-scale convective processes. The anomalously low daily precipitation for nodes 8 and 12 in Figure 8 also supports the reasoning above, that the GDI, a convective precipitation forecasting tool, most accurately resolves the convection-suppressing impacts of the SAL when applied to the Caribbean Basin as opposed to the eastern TNA.

4. Summary and Conclusions

While the Saharan air layer (SAL) is a well-studied feature of the tropical north Atlantic (e.g., Prospero & Carlson, 1972), past work has primarily focused on the evolution of dust loadings during its trans-Atlantic journey (e.g., Chen et al., 2010), its radiative forcing (e.g., Carlson & Benjamin, 1980), or its effect of tropical cyclones (e.g., Dunion & Velden, 2004). However, recent work implicating the SAL in the historic 2015 Caribbean drought (Mote et al., 2017) has further motivated the need to better understand how the convective environment co-evolves with the dust transport to potentially suppress rainfall (Flores et al., 2023; Wong & Dessler, 2005) as the SAL traverses the Caribbean basin. While convective environments in the region reflect the superposition of multiple factors, such as the position and intensity of the NASH, the ITCZ, the Caribbean low-level jet, El Niño-Southern Oscillation phases, etc., this research focuses on the SAL.

In a 40-year classification of common SAL pathways during June and July, this study revealed two recurring SAL patterns characterized by pronounced westward extensions of the dust plume. Composites of the Gálvez-Davison Index (GDI), a convective precipitation forecasting index, on these days revealed a deterioration of the precipitation potential collocated with the dust plume as it migrated away from the west African coast. Meanwhile, composite maps of the daily rainfall anomaly for Puerto Rico revealed island-wide below-average precipitation on the days associated with these most westward-extended SAL configurations. While the direct contribution of the dust via its radiative and microphysical effects to the poor convective environments is unclear at this time, the presence of the elevated hot, dry Saharan air mass is clearly evident among the GDI's inversion index (II) term.

These findings are important for anticipating the implications of future dust outbreaks on water-vulnerable Caribbean islands, such as Puerto Rico. In their thorough analysis of the record-breaking June 2020 SAL outbreak (Figure 7), Pu and Jin (2021) hypothesized that climate model predictions of a stronger and more westward-extended NASH (Li et al., 2011, 2012) would favor more frequent long-range dust transport events, such as the one in June 2020. Indeed, the trend line in Figure 4 indicates a statistically significant increase in SAL outbreaks over the last 40 years, such as the one in June 2020. Integrating these two findings, the Caribbean may face greater water stress during June–July in future decades as a result of more frequent SAL intrusions. Because Puerto Rico's early rainfall season (April–July) is the most hydrologically critical period of the year (Miller et al., 2019), future reductions in June-July rainfall during SAL episodes may disproportionately influence the annual precipitation anomaly (i.e., pluvial vs. drought year).

Such a scenario aligns with both coarse (Karmalkar et al., 2013) and downscaled (Ramseyer et al., 2019) precipitation projections of Puerto Rico's early rainfall season, which project precipitation declines by 2100. Consequently, climate scientists should devote closer attention to the representation of the Saharan dust transport in climate model projections of Caribbean rainfall, which can be a source of struggle, particularly for coarse dust (Adebiyi & Kok, 2020). Meanwhile, water managers in Puerto Rico may monitor dust forecasts and imminent SAL intrusions, which may provide additional lead time, a critical need for anticipating acute water stress events in the eastern Caribbean (Mercado-Díaz et al., 2023).

Data Availability Statement

The SOM node mean IDT, GDI, and precipitation fields and frequencies as well as the IDT node-date pairings (Miller & Ramseyer, 2023) are publicly available at https://doi.org/10.5281/zenodo.10363004.

Acknowledgments
This work was supported by the NOAA Modeling Analysis and Prediction Program award number NA20OAR4310416, and NSF awards 2236655 and 1831952 from the Physical and Dynamic Meteorology program and Division of Environmental Biology, respectively.

References

Adebiyi, A. A., & Kok, J. F. (2020). Climate models miss most of the coarse dust in the atmosphere. *Science Advances*, *6*(15). eaaz9507. https://doi.org/10.1126/sciadv.aaz9507

Alber, K., Zhou, L., & Raghavendra, A. (2021). A shift in the diurnal timing and intensity of deep convection over the Congo Basin during the past 40 years. *Atmospheric Research*, *264*, 105869. https://doi.org/10.1016/j.atmosres.2021.105869

Asutosh, A., Vinoj, V., Murukesh, N., Ramisetty, R., & Mittal, N. (2022). Investigation of June 2020 giant Saharan dust storm using remote sensing observations and model reanalysis. *Scientific Reports*, *12*(1), 6114. https://doi.org/10.1038/s41598-022-10017-1

Carlson, T. N., & Benjamin, S. G. (1980). Radiative Heating rates for Saharan dust. *Journal of the Atmospheric Sciences*, *37*(1), 193–213. https://doi.org/10.1175/1520-0469(1980)037<0193:rhrfsd>2.0.co;2

Chakraborty, S., Guan, B., Waliser, D. E., da Silva, A. M., Uluatam, S., & Hess, P. (2021). Extending the atmospheric river concept to aerosols: Climate and air quality impacts. *Geophysical Research Letters*, *48*(9), e2020GL091827. https://doi.org/10.1029/2020GL091827

Chen, S.-H., Wang, S.-H., & Waylonis, M. (2010). Modification of Saharan air layer and environmental shear over the eastern Atlantic Ocean by dust-radiation effects. *Journal of Geophysical Research*, *115*(D21). https://doi.org/10.1029/2010JD014158

Colarco, P. R., Toon, O. B., Reid, J. S., Livingston, J. M., Russell, P. B., Redemann, J., et al. (2003). Saharan dust transport to the Caribbean during PRIDE: 2. Transport, vertical profiles, and deposition in simulations of in situ and remote sensing observations. *Journal of Geophysical Research*, *108*(D19). https://doi.org/10.1029/2002JD002659

Debbage, N., Miller, P., Poore, S., Morano, K., Mote, T., & Shepherd, J. M. (2017). A climatology of atmospheric river interactions with the southeastern United States coastline. *International Journal of Climatology*, *37*(11), 4077–4091. https://doi.org/10.1002/joc.5000

Doherty, O. M., Riemer, N., & Hameed, S. (2008). Saharan mineral dust transport into the Caribbean: Observed atmospheric controls and trends. *Journal of Geophysical Research*, *113*(D7). https://doi.org/10.1029/2007JD009171

Dunion, J. P. (2011). Rewriting the climatology of the tropical North Atlantic and Caribbean Sea atmosphere. *Journal of Climate*, *24*(3), 893–908. https://doi.org/10.1175/2010JCLI3496.1

Dunion, J. P., & Velden, C. S. (2004). The impact of the Saharan air layer on Atlantic tropical cyclone activity. *Bulletin of the American Meteorological Society*, *85*(3), 353–366. https://doi.org/10.1175/BAMS-85-3-353

Flores, A., Sakai, R. K., Joseph, E., Nalli, N. R., Smirnov, A., Demoz, B., et al. (2023). On Saharan air layer stability and suppression of convection over the northern tropical Atlantic: Case study analysis of a 2007 dust outflow event. *Atmosphere*, *14*(4), 707. https://doi.org/10.3390/atmos14040707

Francis, D., Fonseca, R., Nelli, N., Cuesta, J., Weston, M., Evan, A., & Temimi, M. (2020). The atmospheric drivers of the major Saharan dust storm in June 2020. *Geophysical Research Letters*, *47*(24), e2020GL090102. https://doi.org/10.1029/2020GL090102

Gálvez, J. M., & Davison, M. (2016). The Gálvez-Davison Index for tropical convection. Retrieved from http://www.wpc.ncep.noaa.gov/international/gdi/GDI_Manuscript_V20161021.pdf

Gelaro, R., McCarty, W., Suárez, M. J., Todling, R., Molod, A., Takacs, L., et al. (2017). The Modern-Era Retrospective analysis for research and applications, version 2 (MERRA-2). *Journal of Climate*, *30*(14), 5419–5454. https://doi.org/10.1175/JCLI-D-16-0758.1

Glenn, E. (2022). On a new framework for detecting, classifying, and forecasting floods for large-scale flood risk analysis (Ph.D). *The City College of New York, United States – New York*, 28962303. Retrieved from https://www.proquest.com/dissertations-theses/on-new-framework-detecting-classifying/docview/2624634148/se-2

Guan, B., & Waliser, D. E. (2015). Detection of atmospheric rivers: Evaluation and application of an algorithm for global studies. *Journal of Geophysical Research: Atmospheres*, *120*(24), 12514–12535. https://doi.org/10.1002/2015JD024257

Herrera, D., & Ault, T. (2017). Insights from a new high-resolution drought Atlas for the Caribbean spanning 1950–2016. *Journal of Climate*, *30*(19), 7801–7825. https://doi.org/10.1175/JCLI-D-16-0838.1

Hersbach, H., Bell, B., Berrisford, P., Hirahara, S., Horányi, A., Muñoz-Sabater, J., et al. (2020). The ERA5 global reanalysis. *Quarterly Journal of the Royal Meteorological Society*, *146*(730), 1999–2049. https://doi.org/10.1002/qj.3803

Hewitson, B., & Crane, R. (2002). Self-organizing maps: Applications to synoptic climatology. *Climate Research*, *22*(1), 13–26. https://doi.org/10.3354/cr022013

Huang, J., Zhang, C., & Prospero, J. M. (2010). African dust outbreaks: A satellite perspective of temporal and spatial variability over the tropical Atlantic Ocean. *Journal of Geophysical Research*, *115*(D5). https://doi.org/10.1029/2009JD012516

Huffman, G., Bolvin, D., Braithwaite, D., Hsu, K., Joyce, R., & Xie, P. (2014). Integrated Multi-satellitE Retrievals for GPM (IMERG). Version 4.4. Retrieved from ftp://arthurhou.pps.eosdis.nasa.gov/gpmdata/

Karmalkar, A. V., Taylor, M. A., Campbell, J., Stephenson, T., New, M., Centella, A., et al. (2013). A review of observed and projected changes in climate for the islands in the Caribbean. *Atmósfera*, *26*(2), 283–309. https://doi.org/10.1016/s0187-6236(13)71076-2

Kohonen, T. (1990). The self-organizing map. *Proceedings of the IEEE*, *78*(9), 1464–1480. https://doi.org/10.1109/5.58325

Kuciauskas, A. P., Xian, P., Hyer, E. J., Oyola, M. I., & Campbell, J. R. (2017). Supporting weather forecasters in predicting and monitoring Saharan air layer dust events as they impact the greater Caribbean. *Bulletin of the American Meteorological Society*, *99*(2), 259–268. https://doi.org/10.1175/BAMS-D-16-0212.1

Li, W., Li, L., Fu, R., Deng, Y., & Wang, H. (2011). Changes to the North Atlantic subtropical high and its role in the intensification of summer rainfall variability in the southeastern United States. *Journal of Climate*, *24*(5), 1499–1506. https://doi.org/10.1175/2010jcli3829.1

Li, W., Li, L., Ting, M., & Liu, Y. (2012). Intensification of Northern Hemisphere subtropical highs in a warming climate. *Nature Geoscience*, *5*(11), 830–834. https://doi.org/10.1038/ngeo1590

Lobato, R. R. D. C. (2019). Avaliação do índice termodinâmico Gálvez-Davison na previsibilidade pluviométrica na cidade de Belém-PA. (MS). *Universidade Federal do Pará, Belém, Brazil*. Retrieved from https://bdm.ufpa.br:8443/jspui/handle/prefix/3096

Meng, L., Gao, H. W., Yu, Y., Yao, X. H., Gao, Y., Zhang, C., & Fan, L. (2017). A new approach developed to study variability in North African dust transport routes over the Atlantic during 2001–2015. *Geophysical Research Letters*, *44*(19), 10026–010035. https://doi.org/10.1002/2017GL074478

Mercado-Díaz, J. A., Holupchinski, E., Álvarez-Berríos, N., Gould, W. A., Miller, P., Mote, T., et al. (2023). Fostering knowledge exchange and collaboration among drought-related initiatives in the Caribbean. *Bulletin of the American Meteorological Society*, *104*(6), E1146–E1153. https://doi.org/10.1175/bams-d-23-0054.1

Miller, P., Mote, T., & Ramseyer, C. (2019). An empirical study of the relationship between seasonal precipitation and thermodynamic environment in Puerto Rico. *Weather and Forecasting*, *34*(2), 277–288. https://doi.org/10.1175/waf-d-18-0127.1

Miller, P., & Ramseyer, C. (2020). Did the climate forecast system anticipate the 2015 Caribbean drought? *Journal of Hydrometeorology*, *21*(6), 1245–1258. https://doi.org/10.1175/jhm-d-19-0284.1

Miller, P., & Ramseyer, C. (2023). Recurring trans-Atlantic dust pathways during June-July. https://doi.org/10.5281/zenodo.10363004

Miller, P., Williams, M., & Mote, T. L. (2021). Modeled atmospheric optical and thermodynamic responses to an exceptional trans-Atlantic dust outbreak. *Journal of Geophysical Research: Atmospheres*, *126*(5), e2020JD032909. https://doi.org/10.1029/2020jd032909

Moraes, F. D. S., Mote, T. L., & Seymour, L. (2022). Ocean–atmosphere variability and drought in the insular Caribbean. *International Journal of Climatology*, *42*(10), 5016–5037. https://doi.org/10.1002/joc.7517

Mote, T. L., Ramseyer, C. A., & Miller, P. W. (2017). The Saharan air layer as an early rainfall season suppressant in the Eastern Caribbean: The 2015 Puerto Rico drought. *Journal of Geophysical Research: Atmospheres*, *122*(20), 10966–910982. https://doi.org/10.1002/2017JD026911

O'Gorman, P. A., & Dwyer, J. G. (2018). Using machine learning to Parameterize moist convection: Potential for modeling of climate, climate change, and extreme events. *Journal of Advances in Modeling Earth Systems*, *10*(10), 2548–2563. https://doi.org/10.1029/2018MS001351

Pedregosa, F., Varoquaux, G., Gramfort, A., Michel, V., Thirion, B., Grisel, O., et al. (2011). Scikit-learn: Machine learning in Python. *The Journal of Machine Learning Research*, *12*, 2825–2830.

Pineda-Martínez, L. F., León-Cruz, J. F., & Carbajal, N. (2020). Analysis of severe storms and tornado formation in the northern region of Mexico. *Revista Biociencias*, *7*(e885).

Prospero, J. M., & Carlson, T. N. (1972). Vertical and areal distribution of Saharan dust over the western equatorial North Atlantic Ocean. *Journal of Geophysical Research*, *77*(27), 5255–5265. https://doi.org/10.1029/JC077i027p05255

Pu, B., & Jin, Q. (2021). A record-breaking trans-Atlantic African dust plume associated with atmospheric circulation extremes in June 2020. *Bulletin of the American Meteorological Society*, *102*(7), E1340–E1356. https://doi.org/10.1175/bams-d-21-0014.1

Ramseyer, C., & Miller, P. (2021). Historical trends in the trade wind inversion in the tropical North Atlantic Ocean and Caribbean. *International Journal of Climatology*, *41*(12), 5752–5765. https://doi.org/10.1002/joc.7151

Ramseyer, C., Miller, P., & Mote, T. (2019). Future precipitation variability during the early rainfall season in the El Yunque National Forest. *Science of the Total Environment*, *661*, 326–336. https://doi.org/10.1016/j.scitotenv.2019.01.167

Ramseyer, C., & Mote, T. L. (2018). Analysing regional climate forcing on historical precipitation variability in Northeast Puerto Rico. *International Journal of Climatology*, *38*(S1). https://doi.org/10.1002/joc.5364

Ramseyer, C. A., & Miller, P. W. (2023). Atmospheric flash drought in the Caribbean. *Journal of Hydrometeorology*, *24*(12), 2177–2189. https://doi.org/10.1175/jhm-d-22-0226.1

Reusch, D. B., Alley, R. B., & Hewitson, B. C. (2005). Relative performance of self-organizing maps and principal component analysis in pattern extraction from synthetic climatological data. *Polar Geography*, *29*(3), 188–212. https://doi.org/10.1080/789610199

Rittmeister, F., Ansmann, A., Engelmann, R., Skupin, A., Baars, H., Kanitz, T., & Kinne, S. (2017). Profiling of Saharan dust from the Caribbean to western Africa – Part 1: Layering structures and optical properties from shipborne polarization/Raman lidar observations. *Atmospheric Chemistry and Physics*, *17*(21), 12963–12983. https://doi.org/10.5194/acp-17-12963-2017

Sheridan, S. C., & Lee, C. C. (2011). The self-organizing map in synoptic climatological research. *Progress in Physical Geography: Earth and Environment*, *35*(1), 109–119. https://doi.org/10.1177/0309133310397582

Thornton, P., Running, S. W., & White, M. A. (1997). Generating surfaces of daily meteorological variables over large regions of complex terrain. *Journal of Hydrology*, *190*(3), 214–251. https://doi.org/10.1016/s0022-1694(96)03128-9

Thornton, P., Thornton, M. M., Mayer, B. W., Wei, Y., Devarakonda, R., Vose, R. S., & Cook, R. B. (2017). Daymet: Daily surface weather data on a 1-km grid for North America.

Torres-Valcárcel, A. R. (2018). Teleconnections between ENSO and rainfall and drought in Puerto Rico. *International Journal of Climatology*, *38*(S1), e1190–e1204. https://doi.org/10.1002/joc.5444

Tsamalis, C., Chédin, A., Pelon, J., & Capelle, V. (2013). The seasonal vertical distribution of the Saharan Air Layer and its modulation by the wind. *Atmospheric Chemistry and Physics*, *13*(22), 11235–11257. https://doi.org/10.5194/acp-13-11235-2013

Tucker, C. J., Dregne, H. E., & Newcomb, W. W. (1991). Expansion and contraction of the Sahara desert from 1980 to 1990. *Science*, *253*(5017), 299–300. https://doi.org/10.1126/science.253.5017.299

USDM. (2020). U.S. Drought Monitor. Retrieved from https://droughtmonitor.unl.edu/

Watt-Meyer, O., Brenowitz, N. D., Clark, S. K., Henn, B., Kwa, A., McGibbon, J., et al. (2021). Correcting weather and climate models by machine learning nudged historical simulations. *Geophysical Research Letters*, *48*(15), e2021GL092555. https://doi.org/10.1029/2021GL092555

Wong, S., & Dessler, A. E. (2005). Suppression of deep convection over the tropical North Atlantic by the Saharan air layer. *Geophysical Research Letters*, *32*(9). https://doi.org/10.1029/2004GL022295

Yu, H., Tan, Q., Zhou, L., Zhou, Y., Bian, H., Chin, M., et al. (2021). Observation and modeling of the historic "Godzilla" African dust intrusion into the Caribbean Basin and the southern US in June 2020. *Atmospheric Chemistry and Physics*, *21*(16), 12359–12383. https://doi.org/10.5194/acp-21-12359-2021